Geophysical Journal International

Geophys. J. Int. (2016) **207,** 1244–1257
Advance Access publication 2016 September 4
GJI Seismology

doi: 10.1093/gji/ggw331

Joint relative location of earthquakes without a pre-defined velocity model: an example from a peculiar seismic cluster on Katla volcano's south-flank (Iceland)

G. Sgattoni,[1,2,3] Ó. Gudmundsson,[3] P. Einarsson[2] and F. Lucchi[1]

[1]*Department of Biological, Geological and Environmental Sciences, University of Bologna, Bologna, Italy. E-mail: giulia.sgattoni2@unibo.it*
[2]*Institute of Earth Sciences, Science Institute, University of Iceland, Reykjavik, Iceland.*
[3]*Department of Earth Sciences, Uppsala University, Uppsala, Sweden*

Accepted 2016 September 1. Received 2016 July 20; in original form 2016 February 23

SUMMARY

Relative location methods are commonly used to precisely locate earthquake clusters consisting of similar waveforms. Repeating waveforms are often recorded at volcanoes, where, however, the crust structure is expected to contain strong heterogeneities and therefore the 1-D velocity model assumption that is made in most location strategies is not likely to describe reality. A peculiar cluster of repeating low-frequency seismic events was recorded on the south flank of Katla volcano (Iceland) from 2011. As the hypocentres are located at the rim of the glacier, the seismicity may be due to volcanic or glacial processes. Information on the size and shape of the cluster may help constraining the source process. The extreme similarity of waveforms points to a very small spatial distribution of hypocentres. In order to extract meaningful information about size and shape of the cluster, we minimize uncertainty by optimizing the cross-correlation measurements and relative-location process. With a synthetic test we determine the best parameters for differential-time measurements and estimate their uncertainties, specifically for each waveform. We design a location strategy to work without a pre-defined velocity model, by formulating and inverting the problem to seek changes in both location and slowness, thus accounting for azimuth, take-off angles and velocity deviations from a 1-D model. We solve the inversion explicitly in order to propagate data errors through the calculation. With this approach we are able to resolve a source volume few tens of metres wide in horizontal directions and around 100 metres in depth. There is no suggestion that the hypocentres lie on a single fault plane and the depth distribution indicates that their source is unlikely to be related to glacial processes as the ice thickness is not expected to exceed few tens of metres in the source area. Our method is designed for a very small source region, allowing us to assume a constant slowness for the whole cluster and to include the effects of 3-D heterogeneity such as refraction. Similar circumstances may arise in other volcanic regions with a high level of heterogeneity and where densely clustered earthquakes are often recorded.

Key words: Inverse theory; Volcano seismology; Wave propagation.

1 INTRODUCTION

Earthquake multiplets consist of very similar waveforms, often exceeding cross-correlation coefficients of 0.8 (Geller & Mueller 1980; Frémont & Malone 1987). They are common in tectonic and volcanic areas worldwide and they are likely to be caused by earthquakes occurring very close to each other and generated by similar, non-destructive, source processes (Geller & Mueller 1980). Because they consist of closely-spaced earthquakes, it is possible to determine joint hypocentre locations with high accuracy (Poupinet *et al.* 1984; Fréchet 1985; Frémont & Malone 1987; Got *et al.* 1994; Slunga *et al.* 1995; Waldhauser & Ellsworth 2000; Thelen *et al.* 2008). The method is based on the idea that closely-spaced events recorded at a common station will share similar path effects and site effects. If the hypocentral separation between two events is small compared to the station-hypocentre distance and scale length of velocity heterogeneities, and if these are large compared to the dominant wavelength of the waveforms, then the ray paths to a common station are similar and the relative time lag between the two events will depend on their spatial offset in the direction of the station (Waldhauser & Ellsworth 2000; Wolfe 2002).

Moreover, the location precision is improved by using high-precision waveform cross-correlation methods to determine the relative time measurements. This is possible because of a high degree of similarity between waveforms that contain significant structure at high frequency. This can be done either in the frequency domain (Poupinet *et al.* 1984) or in the time domain (Deichmann & Garcia-Fernandez 1992). The accuracy of the arrival-time differences between pairs of similar events is reported to be on the order of 0.001 s for micro-earthquakes recorded by local networks (e.g. Frémont & Malone 1987). This makes it possible to calculate the relative location between hypocentres with uncertainty on the order of a few metres to tens of metres (Waldhauser & Ellsworth 2000).

This is particularly useful at volcanoes, where earthquakes are often characterized by unclear phase onsets and their arrival-time determination can be highly imprecise with manual phase-picking. The relative location of earthquake multiplets is, therefore, a common practice at volcanoes worldwide, e.g. at Kilauea (Got *et al.* 1994), Montserrat (Rowe *et al.* 2004), Mount St. Helens (Thelen *et al.* 2008).

Two techniques are commonly used for relative location of earthquakes. One is the master-event approach, where all other events are relocated with respect to one, the master event (ITO 1985; Scherbaum & Wendler 1986; Frémont & Malone 1987; VanDecar & Crosson 1990; Deichmann & Garcia-Fernandez 1992; Lees 1998). Alternatively, cross-correlation time delays can be computed for all possible event pairs and combined in a system of linear equations to determine hypocentroid separations (Got *et al.* 1994; Waldhauser & Ellsworth 2000). In addition to adding more constraints to the model parameters, this strategy makes it possible to increase the spatial extent of the cluster that can be relocated, as there is no need for all events to correlate with the master.

The ability of the relative-location technique to recover the relative locations well depends on (i) the geometry of the network, (ii) the accuracy of differential-time measurements, (iii) the deviations from the assumption that the ray paths do not change within the cluster of events, (iv) the direction of the rays leaving the source, depending on 3-D velocity variations (Slunga *et al.* 1995; Michelini & Lomax 2004). The problem is usually solved in a 1-D velocity model (e.g. Waldhauser & Ellsworth 2000) or with a constant slowness vector for each station to the cluster (Got *et al.* 1994). However, in these approaches the source of error represented by the uncertainties in the ray directions in the source volume is not taken into account. Michelini & Lomax (2004) showed how the initial 1-D velocity model used, determining the take-off angles, influences the resulting shape of the relocated cluster. Moreover, in highly heterogeneous media, such as in volcanic areas, strong lateral heterogeneities can cause considerable deviations in the direction of the seismic rays from the straight path assumed in a 1-D velocity model. This, in turn, can affect the spatial direction in which the earthquake location is re-adjusted as constrained by each station's differential time.

We propose a relative location strategy that does not rely on a 1-D velocity model, but rather seeks changes in slowness vectors together with changes in relative location of hypocentres. We apply this technique to a cluster of LP (Long Period; Chouet 2003) seismic events located on the south flank of the subglacial volcano Katla, in south Iceland. This cluster is described in detail by Sgattoni *et al.* (2016). This seismicity started in 2011, in association with an unrest episode which culminated in a glacial flood. Seismic events in this part of Katla volcano had not been recorded before. Since they occur in a glaciated area, they can be generated by either glacial or volcanic processes. Sgattoni *et al.* (2016) suggested that they are associated with shallow hydrothermal processes. A closer insight into the relative location of the hypocentres can give a useful contribution to the source interpretation.

The extreme similarity of the waveforms indicates a very small spatial distribution of the hypocentres and a very similar source process for all of the events. Moreover, indications of strong path effects, together with the poorly known velocity model for the site, motivated the development of a specific strategy to optimize both the differential-time measurements and the relative location technique. We conduct both cross-correlation measurements and relative-location inversion so that the uncertainty is carefully estimated and the sources of error minimized in each step. We perform a statistical test to evaluate the best cross-correlation parameters and uncertainties of differential-time measurements specifically for each station and each seismic phase used. This alleviates the need to use generalized statistical assumptions about errors. We then relocate the events with a master-event location strategy, inverting for both changes in location and in slowness, in order to account for azimuth, take-off angles and velocity deviations from a 1-D model. We solve the inversion explicitly in order to propagate data errors through the calculation. We also perform synthetic tests to evaluate the ability of this approach to recover relative locations and slowness-vector components.

2 SEISMIC DATA

2.1 Seismic network

Following the eruptions of the neighbouring Eyjafjallajökull volcano in 2010, the Icelandic Meteorological Office (IMO) augmented the seismic monitoring network around Katla from five to nine stations. Moreover, nine temporary stations were deployed by Uppsala University between July 2011 and August 2013. Because the seismic events we analyse are very small (magnitude lower than 1.2; Sgattoni *et al.* 2016), the signal to noise ratio (snr) is low at distant stations. Therefore, we used data from 13 out of 19 stations (Fig. 1). The equipment at each station is listed in Table 1. Data were recorded at 100 Hz. Stations were powered with batteries, wind generators and solar panels. All the instruments recorded in continuous mode, but some technical problems (e.g. power failure) mainly due to harsh weather conditions (especially in winter time), prevented some stations from working continuously during the whole operation time.

2.2 LP seismic events, Katla south flank

The LP events recorded near Gvendarfell on Katla's south flank have been described in detail by Sgattoni *et al.* (2016). We report here the main features. The seismicity is shallow and located on the southern side of the Mýrdalsjökull glacier. It is characterized by small magnitude (~ -0.5–1.2 M_L), long-period earthquakes with an emergent *P* wave and an unclear *S* wave (Fig. 2). The frequency content is narrow banded around 3 Hz at most stations (Fig. 2). All events have remarkably similar, nearly identical waveforms with correlation coefficient ≥ 0.9 at the nearest stations, throughout the whole time period investigated (March 2011 - August 2014). The detected size distribution has two peaks, at small events below magnitude $M_L = 0.2$ and bigger events with magnitude between $M_L = 0.2$ and $M_L = 1.2$.

The signals are characterized by a number of distinct seismic phases, which nature is difficult to understand, as the waveforms are

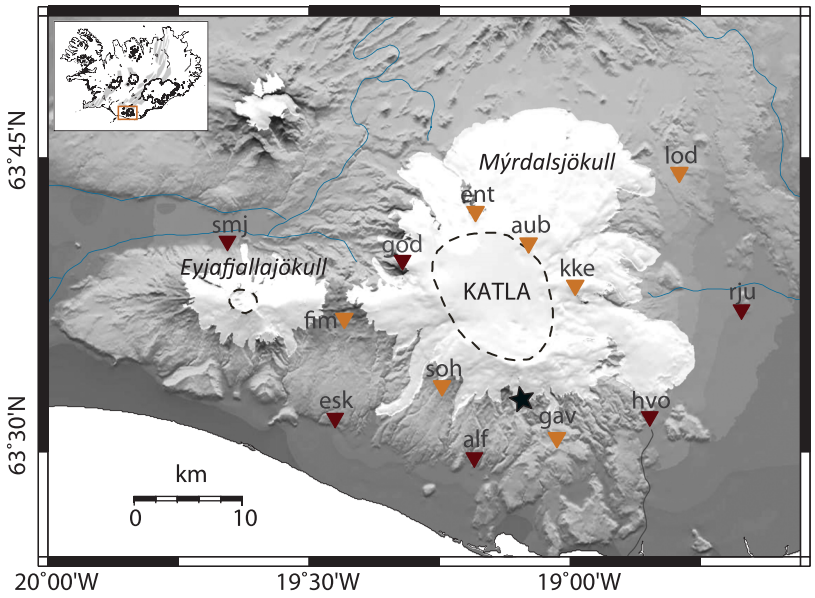

Figure 1. Map of Mýrdalsjökull and Eyjafjallajökull showing the seismic network used in this study. Dark brown triangles: permanent IMO seismic stations. Orange triangles: temporary Uppsala University seismic stations operating between July 2011 and August 2013. The star marks the new Gvendarfell cluster on the south flank. The Katla and Eyjafjallajökull caldera rims are outlined by dashed lines. White areas are glaciers. Topography information from National Land Survey of Iceland.

Table 1. Instrumentation used at all 13 seismic stations used in this study.

	Sensor	Digitizer
ALF	GURALP ESPA	GURALP
GOD	GURALP ESPA	GURALP
RJU	GURALP ESPA	GURALP
SMJ	GURALP ESPA	GURALP
GAV	GURALP CMG3	GURALP
SOH	GURALP CMG3	GURALP
FIM	GEOTECH KS-2000	REFTEK
ESK	Lennartz 5s	GURALP
HVO	Lennartz 5s	GURALP
AUB	Lennartz 5s	REFTEK
ENT	Lennartz 5s	REFTEK
KKE	Lennartz 5s	REFTEK
LOD	Lennartz 5s	REFTEK

apparently contaminated by secondary phases generated by strong path effects based on their particle motion diagrams (not presented here). It is in general possible to recognize a *P* phase and a secondary wave package which interpretation is less clear, probably containing both S waves and surface waves. Although unclear, we will refer to it as an *S* wave (Fig. 2).

Around 1800 events have been detected with cross-correlation of a sample waveform with continuous data between July 2011 and August 2013. The temporal evolution shows striking features during the whole period investigated (July 2011–August 2013): events occur with regular time intervals, modulated by a seasonal variation. A maximum event rate of 6-8 events per day is observed in late summer and a minimum rate of 1 event every 1–2 d in winter. This regular temporal pattern started a few hours before a 23 hr tremor burst that originated in the southeastern sector of the caldera on July 8–9, 2011 (Sgattoni *et al.* 2016). No visible eruption occurred on the glacier, but the tremor was associated with intensified earthquake activity within the caldera and a glacial flood that drained from the southeast rim of the Mýrdalsjökull glacier and caused damage to infrastructure.

Because of the features of the glacier (small and stagnant), temporal association with unrest, repetitivity of waveforms and peculiar temporal pattern, Sgattoni *et al.* (2016) suggested that this seismicity is associated with hydrothermal processes, although no source manifestation of geothermal activity is visible in the area.

3 DIFFERENTIAL TIME MEASUREMENTS

As all the waveforms are extremely well correlated, we expect a very small spatial distribution of hypocentres. We can crudely estimate the maximum size of the source distribution by requiring a phase difference of less than a fraction of a period in order to achieve such high levels of correlation. Taking this fraction to be a quarter and assuming an average velocity of 3.5 km s^{-1} and a dominant frequency of 3.5 Hz, we constrain the source region to be smaller than 250 m in size. Therefore, in all steps leading to the relative location results, we attempt to minimize the uncertainty and also carefully estimate it, from the differential-time measurements to the resulting relative locations. In order to measure the relative times as accurately as possible, we set up a synthetic test to identify the best parameters to use for the cross-correlation. With the same synthetic test we also evaluate their uncertainty, later used as weights for the relative location inversion.

3.1 Statistical test for cross-correlation

We conduct a synthetic test where the time shifts between a clean waveform (the template waveform) and the same waveform with different levels of random noise added are measured. The random noise is filtered white noise with the same filter as the template and adjusted in amplitude to match a specific snr, which is defined as the ratio between the root-mean-square (rms) signal amplitude in the correlation time-window and rms noise amplitude in a window of equal length before the *P* arrival.

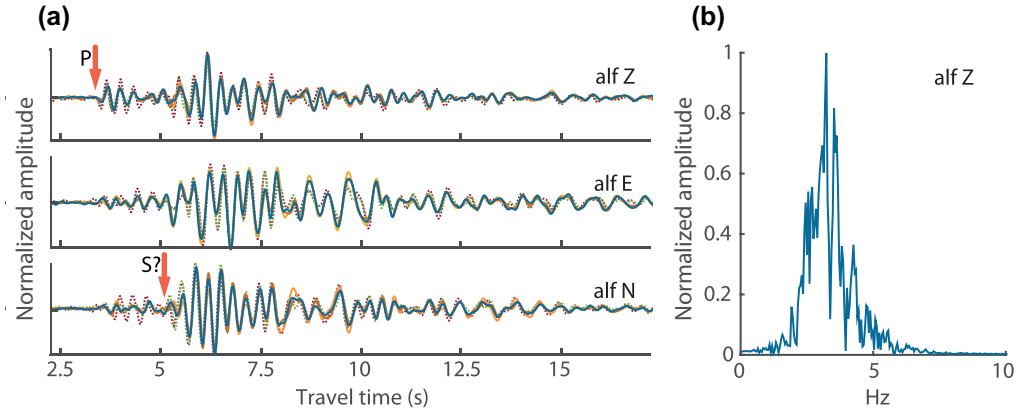

Figure 2. (a) Example seismograms of five Gvendarfell events at stations ALF (with correlation coefficient > 0.95). Solid lines correspond to three events recorded before August 2012 and dashed lines are two events recorded after that. (b) Normalized amplitude spectra of the Z component of one event at station ALF.

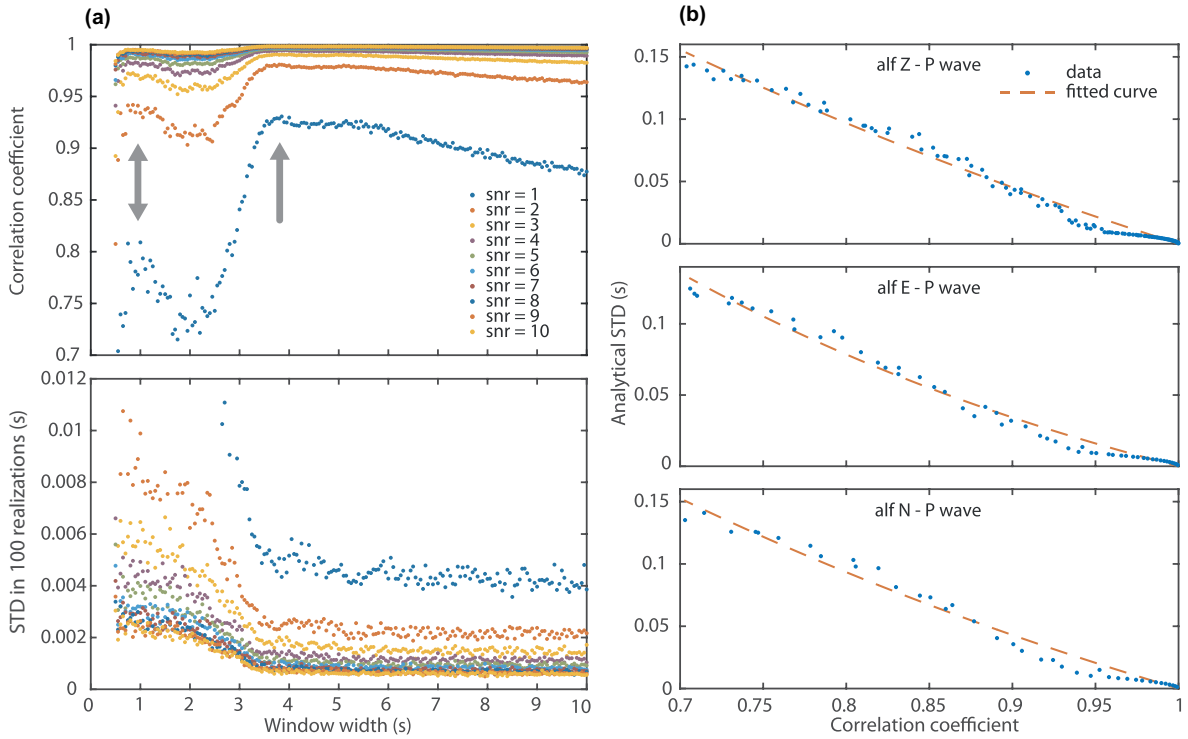

Figure 3. Statistical simulation to determine uncertainty of cross-correlation measurements. Data from station ALF. (a) correlation coefficient and std obtained for different widths of the window used for correlation and different values of snr. Window widths are measured starting from *P* arrival time. A first peak is observed at around 1 s (double arrow): this is the width chosen for *P* wave. At station ALF the *S*–*P* time is 1.6 s and this determined increase in correlation after this time and reaching a new peak at 4 s (single arrow). The window width chosen for *S* wave is therefore 2.4 s (corresponding to 4 s minus 1.6 s). As expected, uncertainty decreases with increasing snr. (b) Analytical std as a function of correlation coefficient, measured for chosen window width (1 s) and varying snr. Results for three components of *P* wave at ALF. An empirical fitted curve is then used to estimate uncertainty of differential-time measurements between the template event and all the others.

At each station and for each component of the signal:

(1) *P* and *S* phases are identified and extracted from the template waveform, previously band-pass filtered between 2–4, 1–5 or 2–5 Hz depending on the station (the *S* phase is identified only at stations ALF, GAV, SOH, HVO, ESK, FIM and RJU);

(2) The extracted *P*/*S* window is tapered with a 10 per cent cosine taper;

(3) A template *P*/*S* window is correlated in the time domain with the same window with noise added (without applying any time shift so that the differential time is known to be exactly zero). A parabolic interpolation around the peak of the correlation function is done to estimate the time shift with sub-sample precision;

(4) The test is repeated for different snr, varying from 1 to 10, and different widths of the *P* and *S* windows, from 0.5 s to a few seconds.

The whole process is performed at least 100 times, each time generating a new random noise vector (Fig. 3). The std (standard deviation) of the calculated time shifts is then computed and its behaviour is analysed to determine, for each station, (i) the best window width to use for each type of wave and component at

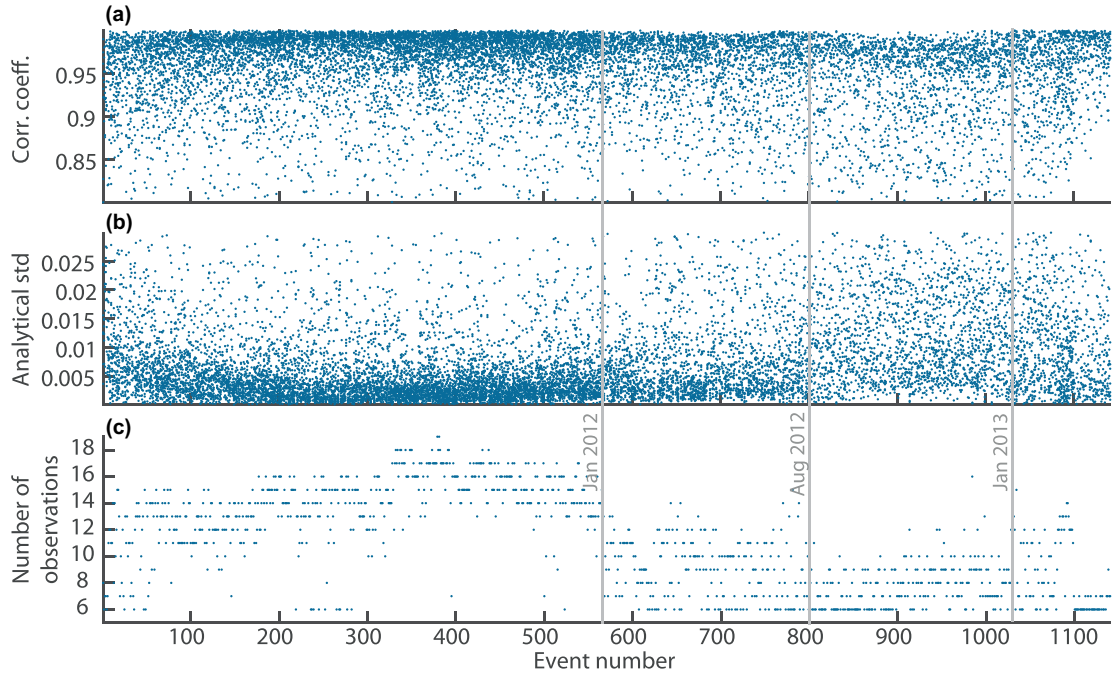

Figure 4. Correlation coefficient (a), analytical error std (b), and number of observations for each event used in the relative location (c). Changes with time are highlighted with time-labelled vertical bars.

each station, (ii) the expected std as a function of the correlation coefficient. The first is done as follows:

(1) The correlation coefficients obtained for different snr and window widths are plotted against the window width used, always starting at the *P* arrival time at a given station;
(2) Two peaks are identified in this plot. One peak occurs before the *S* arrival and represents the best window length for the *P* wave. The other peak occurs after the *S* arrival and corresponds to the sum of *P* and *S* windows that have best correlation. The best window width for the *S* wave, therefore, corresponds to the time of the second peak minus the *S*–*P* time at a given station.

Fig. 3 shows an example for station ALF: a first peak of correlation is observed at 1 s and this is, therefore, the width chosen for the *P* wave. At this station the *S* phase arrives 1.6 s after the *P* phase and this is reflected by an increase in correlation coefficient starting after this time and reaching a new peak around 4 s. Therefore, the window width chosen for the S wave is 2.4 s.

The analytical std as a function of the correlation coefficient is then estimated for the chosen window length (Fig. 3):

(1) The std obtained for different snr and window lengths is plotted as a function of correlation coefficient;
(2) An empirical curve is fitted to the data and later used to estimate the uncertainty of the differential-time measurements of the real data, based on the correlation coefficient.

The same procedure is repeated for *P* and *S* phases and all components. The uncertainty of the differential time estimates is in most cases lower than the sampling interval (0.01 s) and as low as 1 ms (Fig. 4).

This synthetic test allows for optimization of the differential-time measurements in order to minimize uncertainty. It also allows us to estimate uncertainty specifically for each waveform, thus avoiding further generalized statistical assumptions about errors.

3.2 Cross-correlation measurements

Once the best parameters for the time-difference estimation are determined, a cross-correlation scheme is built to correlate a reference event (later used as master event for the relative location) with all other events (*P* and *S* phases separately), at all stations, for all components. Sub-sample estimates of time lags are achieved in the time domain through polynomial interpolation of the cross-correlation coefficient peak. Since not all stations have been working at the same time for the entire period of study, it is not possible to identify one unique reference event. An event which occurred on 2011 October 10 is chosen for stations ALF, GAV, KKE, HVO, AUB, ENT, RJU, ESK, FIM, SLY, SMJ. An event on 2013 February 18 is chosen for SOH and on 2011 October 1 for LOD.

For each station, the differential-arrival times and the corresponding uncertainties are estimated for *P* and *S* waves for all three components. Moreover, we compute for each phase (*P* and *S*) the weighted average of the time shifts for the different components, weighted by their uncertainty. Ultimately, the best estimates (in terms of low error) are selected between the four values obtained (three components and weighted average) and the uncertainty used to weight the data in the relative-location inversion.

The cross-correlation times are selected by setting a lower threshold for the cross-correlation coefficient as high as 0.9 for the closest stations and 0.8 for more distant stations and only event pairs with at least six time measurements are used (Fig. 4). We also discard some outlying data, with uncertainty greater than 0.03 s. This reduces the number of relocated events to 1140. This is mainly due to the small magnitude of the events, in particular the smaller-magnitude group, which is only observed at a few nearby stations. From around August 2012 a decrease in average magnitude from 1 M_L to 0.5 M_L is also observed for the larger-magnitude group of events (Sgattoni *et al.* 2016). There is a greater loss of data in the second part of the data set, after January 2012, when a slight decrease of correlation coefficient occurs and some data are lost due to technical

problems at some seismic stations (Fig. 4). The decreased correlation coefficient causes increased uncertainty of differential-time measurements (Fig. 4), which starts in January 2012, increases until August 2012 and remains fairly stable after that. Consequent deterioration of location quality (discussed later) can thus be traced to this temporal evolution of snr and magnitude. Two example waveforms recorded after August 2012 are reported in Fig. 2 to show the slight decrease in correlation.

4 RELATIVE-LOCATION METHOD

As no catalogue locations exist for all 1200 events, a strategy is used to relocate the events starting from the same initial location and relocating them with respect to the fixed location of a master event (ITO 1985; Scherbaum & Wendler 1986; Frémont & Malone 1987; VanDecar & Crosson 1990; Deichmann & Garcia-Fernandez 1992; Lees 1998). An event which occurred on 2011 October 10, used as reference for cross-correlation time measurements at most of the stations, is chosen as a master event. As location coordinates, we use the non-linear location results obtained by Sgattoni *et al.* (2016). Since a different reference event was used for cross-correlation measurements at stations SOH and LOD, we made sure that the three reference events used had at least eight differential time information linking them.

In the first instance, the routine is built to relocate events in a 1-D velocity model, similar to most relative-location strategies (e.g. Slunga *et al.* 1995; Waldhauser & Ellsworth 2000). However, the data misfit achieved is not satisfactory, as the data are not explained by the model locations close enough to their level of uncertainty (known from the synthetic test explained above). The misfit, normalized by the data covariance, exceeds the expectation of the chi-squared distribution by a factor of 5.

We think this is partially due to effects of lateral heterogeneities that are expected to be strong in the crust in the area and may cause considerable deviations in the direction of the seismic rays from the straight path assumed in a 1-D velocity model. Since this direction can vary considerably because of the local heterogeneities, this introduces inconsistencies that cannot be explained by the model. In addition, the correlation-time measurements are integrated measurements of wave packages extending over 0.5 to several seconds. They are likely to contain waves of varying type and geometry due to scattering. This is confirmed by their complex particle motion. Therefore, the effective slowness of these waves as they leave their source may differ from that predicted by a simple 1-D model, in terms of azimuth, incidence angle and effective local velocity. Thus, the strategy is adjusted to account for this and the slowness vectors (three spatial components per station per wave type) are included as model parameters in the inversion. Azimuths, incident angles and P/S velocity are allowed to be modified by the inversion, in order to account for effects of velocity heterogeneities.

One effect that we have not considered, but may affect our inability to fit the data within their analytical errors is a possible phase shift due to propagation over a finite source. This time shift can be described for coherent rupture over a planar fault by $\Delta t \simeq L/c$, where L is the distance over which rupture propagates and c is wave-propagation speed. We estimate this time shift by extrapolating earthquake-scaling laws to the low magnitude of our events ($M_L = 1$; Sgattoni *et al.* 2016), to potentially be on the order of 10 ms. This is large compared to the uncertainty of our differential times. However, we do not know that the above model describes our sources. If such an effect were coherent for all events in our cluster, then it would cancel in our measurements. If the effect were random for all of our sources, its variation from one event to another would likely be considerably smaller than its maximum potential size. If it were geometrically systematic within the cluster that would be absorbed by the slowness vectors for the different stations. This phase shift would be associated with a significant Doppler effect. If the rupture propagation time shift varied from one event to the other, then we should observe a significant variation of the events' spectra. We observe no such variation. In conclusion, this effect may contaminate our results, but may also help explain why we are not able to explain our data within their uncertainty.

4.1 Formulation of the problem

At a given station, the arrival time, t, for an earthquake, i, corresponds to the sum of the origin time, τ, and the travel time, T, as a function of the event spatial coordinates, $\mathbf{x}_i$:

$$t_i = \tau_i + T(\mathbf{x}_i). \tag{1}$$

We assume the locations are around a point, $\mathbf{x}_0$, with only small changes, $\delta\mathbf{x}_i$, much smaller than the propagation distance:

$$\mathbf{x}_i = \mathbf{x}_0 + \delta\mathbf{x}_i \qquad |\delta\mathbf{x}_i| \ll \text{source} - \text{station distance} \tag{2}$$

If the distances between the events are much smaller than the propagation distance from source to receiver, then the differences in path from the events to the same station can be described as planar. In our example, the distances between source and receiver are in the range of 6–30 km and the events are likely to be generated at distances from the centre of the cloud on the order of $\geq$100–150 m, as apparent from the nonlinear absolute locations presented by Sgattoni *et al.* (2016) and from the extremely similar waveforms. The events are so close to each other that a first order, linear or planar approximation of the traveltime function is justified. Therefore, we can apply a linear approximation:

$$T(\mathbf{x}_i) = T(\mathbf{x}_0 + \delta\mathbf{x}_i) \simeq T(\mathbf{x}_0) + \mathbf{u} \cdot \delta\mathbf{x}_i \tag{3}$$

where $\mathbf{u}$ are linear coefficients (Fréchet derivatives of travel time with respect to change of location) with the unit of slowness (s km^{-1}). Consequently, the differential arrival-time, δt, between events i and j at a given station, can be expressed as:

$$\delta t_{ij} = t_i - t_j = \tau_i - \tau_j + \mathbf{u}(\delta\mathbf{x}_i - \delta\mathbf{x}_j). \tag{4}$$

This is similar to the formulation by Got *et al.* (1994) who used a constant slowness vector for each station to the cluster. Instead, we allow the slowness vector to each station to vary in the inversion. Eq. (4) is non-linear in the last term when both $\mathbf{u}$ and $\delta\mathbf{x}_i$ are unknown and the model parameters are coupled, as they appear as a product. So, we linearize again by differentiating with respect to slowness and location parameters, to seek changes in both slowness and location:

$$\delta t_{ij} \simeq \tau_i\Big|_0 - \tau_j\Big|_0 + d\tau_i - d\tau_j + \mathbf{u}_0(\delta\mathbf{x}_i - \delta\mathbf{x}_j) + \mathbf{u}_0(d\delta\mathbf{x}_i - d\delta\mathbf{x}_j) + d\mathbf{u}(\delta\mathbf{x}_i - \delta\mathbf{x}_j)\Big|_0, \tag{5}$$

where the 0 subscript indicates the initial guess (or estimate at previous iteration) and d indicates the change of the model parameter. In each iteration we solve for perturbation of location parameters (spatial and origin time) and perturbation of the slowness vector, thus obtaining an update of location and slowness. We also apply constraints to the slowness vector within reasonable bounds in order to avoid absurd geometry configurations such as rays leaving the source in opposite direction with respect to the station location.

The initial slowness vector **u** is determined from azimuth angles, α, and incidence angles, φ, for each station j, (estimated in a 1-D velocity model) and constant initial velocities, v, for P/S waves:

$$\mathbf{u}_j = \left(-\sin\alpha_j \sin\varphi_j \frac{1}{v}; -\cos\alpha_j \sin\varphi_j \frac{1}{v}; -\cos\varphi_j \frac{1}{v} \right). \quad (6)$$

The initial P velocity is set as the P velocity at the master event hypocentral depth, corresponding to 3.5 km s^{-1}. The S velocity is set as the P velocity scaled by a factor of $1/\sqrt{3}$. In total, the slowness parameters are six per station (3 for P and 3 for S). We do not constrain the angles to be the same for P and S, as there can be different scattering phenomena with different influence on P and S azimuth and incidence angles.

Our formalism applies two basic assumptions. The first is that of ray theory. The second is that the distances between events in our event cluster are small compared to the distance to the nearest seismograph so that the reciprocal wave front from the station to the cluster has small curvature. The former is possibly questionable in a volcanic setting and this is difficult to evaluate because we do not know the characteristics of small-scale heterogeneity in the region. The potential problem is that scattering effects, which are not accounted for, may be significant. The latter is clearly satisfied (see below).

It is useful to refer to the diagram by Aki & Richards (1980) characterizing scattering problems (their figure 13.11). We note that our events are quite monochromatic at a frequency of 3 Hz. The source region is shallow and near-surface P-wave velocity is expected to be close to 3–3.5 km s^{-1}, while the S-wave velocity is expected to be about 1.7–2.0 km s^{-1}. Thus, the wave number will be $k_P \simeq 6$ km^{-1} and $k_S \simeq 10$ km^{-1} for P and S waves, respectively. The propagation distances to our network stations range from about $L = 6$ km to about $L = 30$ km. Dimensionless propagation distance is, therefore, $k_P L = 36$–180 for P waves and $k_S L = 60$–300 for S waves.

We do not know the characteristic scale of heterogeneity in the region. We do know that the highest resolution tomographic models for the area contain $\simeq$15 per cent velocity heterogeneity on scales larger than about 5 km (Jeddi *et al.* 2016). The dimensionless heterogeneity scale is therefore $k_P a = 30$ for P waves and $k_S a = 50$ for S waves (where a is the characteristic scale of heterogeneity, i.e. 5 km in this case). These numbers place us in the ray-tracing regime of Aki and Richard's diagram. We can speculate that the characteristic scale of heterogeneity is smaller, for example, about 1 km. That would place us in the scattering regime of the diagram. Heterogeneity that is comparable to the dimensions of our event cluster (100 m) would, however, place us at or below the boundary between the scattering regime and the equivalent-homogeneous-medium regime, where our ray-theory assumption becomes valid again. Furthermore, this means that our 3 Hz waves are blind to such small-scale heterogeneity should it exist, which supports our second assumption.

4.2 Inversion

As we do not have catalogue locations for all events, before inverting for relative locations, we need an estimate of origin times. So, we first formulate the problem in order to invert for origin time. This is a linear problem in which the differential arrival times correspond to the sum of the differential origin times and differential travel times:

$$\delta t_{ij} = \tau_i - \tau_j + T(\mathbf{x}_i)\Big|_0 - T(\mathbf{x}_j)\Big|_0. \quad (7)$$

We solve the problem by assuming that all events are located at the master event location (i.e. all relative locations equal to zero). Therefore, the travel times for all events are the same and eq. (7) simplifies to a difference of origin times. We combine all data in a system of linear equations of the form:

$$\mathbf{WGm} = \mathbf{Wd} \quad (8)$$

where **G** is a matrix of size N x Nev (N is the number of differential-time measurements; Nev is the number of events), **m** is the model vector of length Nev, containing origin times, **d** is the data vector of length N, and **W** is a diagonal matrix containing weights.

We then add hard constraints in the form of Lagrange multipliers in order to fix the master event origin time to a reference time (that we set to 0). The problem is overdetermined and can be solved in a weighted least-squares sense, where the weights are set as the inverse of the data covariances:

$$\mathbf{m} = \left[\mathbf{G}^T \mathbf{C}_d^{-1} \mathbf{G}\right]^{-1} \mathbf{G}^T \mathbf{C}_d^{-1} \mathbf{d} \quad (9)$$

where $\mathbf{C_d}$ is the data covariance matrix, a diagonal matrix containing data variances determined by the synthetic tests described in the previous section. In order to determine the inverse of the product matrix $\left[\mathbf{G}^T \mathbf{C}_d^{-1} \mathbf{G}\right]$, we use the singular-value decomposition (SVD) method. The system is well-conditioned and there is no need to regularize.

After solving for the origin time, an iterative process is set up to invert eq. (5) alternatively for relative changes in location, $\left(d\delta\mathbf{x}_i - d\delta\mathbf{x}_j\right)$, and changes in slowness, $d\mathbf{u}$. The inversion strategy is the same as before, but the size of the matrices and the hard constraints change. In the inversion for location parameters, the model vector **m** has length 4Nev ($d\delta\mathbf{x}_1, d\delta\mathbf{x}_2, d\delta\mathbf{x}_3, d\tau$) and the size of **G** is N x 4Nev. The Lagrange multipliers consist in this case of four additional equations to constrain all changes of hypocentral parameters of the master event to be zero. Also in this case, the system is well-conditioned as we pre-filtered the data so that all event pairs have at least six observations. This way all events are well linked to each other.

When inverting for slowness perturbations, the size of the matrices decreases significantly as the number of model parameters reduces to the size of the slowness vector, that is, six times the number of stations (Nst), and **G** is therefore N x 6Nst. Again, the inversion strategy is the same and the matrix is inverted with SVD. In this case, some regularization is needed to exclude the zero eigenvalues originating from stations that have no information for some slowness components, depending on which phases have been used for the cross-correlation. Also, some small eigenvalues can occur if only little information is used for some stations and if, due to the geometry of the problem, some directions are poorly constrained. A threshold value for eigenvalues is found by trial and error.

After the inversion is performed, the resulting perturbations of slowness are checked in order to apply constraints to incidence angle, azimuth and velocity variations, so that they do not exceed specified values. P and S wave velocities are allowed to vary within $\pm$1 km s^{-1} from the initial values. The azimuth angles can change within $\pm$30 degrees from the initial direction and the incidence angles within $\pm$20 degrees.

The inversion scheme is therefore the following:

(1) Iteration 0: inversion for origin time and inversion for location parameters (using the initial slowness vector);
(2) Iteration 1...n: inversion for slowness and inversion for location parameters (using updated slowness vector).

The process is iterated until the misfit reduction is negligible, for a total of seven iterations.

4.3 Model covariance estimation

The uncertainty of the location model parameters is then determined by propagating the estimated data covariances to the model parameters. However, this is sufficient only if the data are appropriately explained (within their uncertainty). In our case study this does not happen, as the final misfit achieved is bigger than the value expected statistically. If data are appropriately explained, the data misfit scaled by data covariance, Q, is expected to equal the number of degrees of freedom of the model, if the model errors are Gaussian:

$$E\{Q\} = \mathbf{e}^T \mathbf{C}_d^{-1} \mathbf{e} = n - r \tag{10}$$

where $E\{Q\}$ is the expectation of Q, $\mathbf{e}$ is the prediction error, n is the number of observations and r is the number of eigenvalues used in the inversion (the degrees of freedom in the model). In our case the misfit is bigger than $(n - r)$. This means that errors in the problem are not fully described by measurement errors. Additional errors occur, possibly due to simplification of the theory or limited knowledge about the velocity model. We account for this by adding a uniform diagonal covariance to our estimated data covariance matrix, so that the expected misfit indicates that data are appropriately explained. We do this by calculating Q as a function of data variance, σ_d^2 , with a constant, c, added to the diagonal elements:

$$\hat{Q} = \mathbf{e}^T \left(\mathbf{C}_d^{-1} + c\mathbf{I}\right)^{-1} \mathbf{e} \tag{11}$$

where $\mathbf{I}$ is the identity matrix. We solve $\hat{Q} = n - r$ for c. We therefore obtain a new data-covariance matrix, which includes both measurement errors and errors due to simplifications of the way the forward problem is described and solved. We use this as a new estimate of the total data covariance and propagate it through the calculation, to estimate the model covariance, that is, the uncertainty of relative location.

This strategy of adding a random component to the data variance estimates of measurement errors assumes that the errors in the data are independent of errors due to the simplification of the forward problem. Another possible strategy would be to scale the errors up according to the residual misfit, but we have no reason to expect that the unaccounted for errors are correlated with and proportional to the analytical measurement errors.

The resulting uncertainty of spatial location parameters is on the order of 15–20 m for the horizontal components and 30–40 m for the vertical. A general increase in uncertainty is observed from January 2012, correlating with bigger data uncertainties (see Section 3.1) and associated with less phases available per event-pair, as explained in Section 3.2.

5 SYNTHETIC TESTS

In order to test the behaviour of the inversion and the ability of the program to recover both hypocentre locations and slowness components, we performed several synthetic tests with the station configuration and geometry of the problem of our case study on the south flank of Katla. Using eq. (4), we generate differential times for all event pairs of a set of 50 events with random hypocentral locations within a 300 × 300 × 300 m^3 volume. The data are generated using an initial slowness vector for the same 1-D model that was used to construct the slowness for the inversion of real data (Section 4.1).

We generate perfect data and a slowness vector perturbed with random Gaussian errors. We track, iteration by iteration, the slowness vector std with respect to the true slowness and the spatial and temporal mislocations of the hypocentres. We repeat the test at least 100 times and compute an ensamble average of the results for all realizations. We repeat the same process for different size initial slowness perturbations. We set the bounds of the constraints imposed during the inversion (Section 4.2) as the maximum perturbation allowed, corresponding to two std of the Gaussian distribution used to generate the random errors. We then perform several tests with decreasing percentages of this maximum perturbation, from 100 per cent to 0.1 per cent. In all tests data are fitted perfectly, while hypocentre locations and slowness components are recovered to some extent, depending on the initial slowness perturbation. The average results for 100 repetitions of this test show that:

(1) the smaller the perturbation of the initial slowness vector the better hypocentre locations are recovered (with perfect recovery for an unperturbed initial slowness vector). For small perturbations, most of the relocations occur at the initial, zeroth iteration. This is expected since in this case the non-linearity is weak (Fig. 5);

(2) the slowness vector (in terms of azimuths, incidence angles and P and S velocity) is adjusted, iteration by iteration, towards the truth, with a reduction of the std (compared to the true slowness) of 50 to 70 per cent achieved (greater proportional reduction when starting with less perturbed slowness, Fig. 5);

(3) when the slowness perturbation applied is small (up to 20 per cent of the maximum perturbation allowed) the hypocentral locations do not change significantly after the initial zeroth iteration, although the slowness vector changes and moves towards the truth (Fig. 5a);

(4) for larger slowness perturbations (up to the maximum), the hypocentral mislocations reduce with iteration, but the mean mislocation reduction (in terms of distance between true and calculated locations) only reaches a maximum on the order of 30–40 per cent for the maximum initial slowness perturbation (Fig. 5b).

These tests demonstrate effects of the non-linearity of the problem and that trade-offs occur between location parameters and the slowness vector. The function we try to minimize has multiple minima that may prevent the inversion from reaching the global minimum. This, in turn, means that the final relative locations obtained may depend on the initial slowness vector. However, the true slowness vector is successfully recovered by at least 50 per cent in all of our tests and, even for the larger initial slowness perturbations, the hypocentre mislocations are significantly reduced also, after the zeroth iteration, when introducing the inversion for slowness.

6 RELATIVE LOCATION RESULTS

Since the synthetic tests demonstrate a trade-off between relative locations and slowness vector, we compute the inversion with different starting slowness vectors and compare the results. We perturb the initial guess of the slowness vector (obtained as described in Section 4.1) with 25 per cent, 50 per cent and 100 per cent of the maximum allowable random perturbation, for a total of eight inversions. All inversions converge to similar results both in terms of relative locations and slowness vectors. The initial misfit (after inversion for origin time), normalized by the data covariance and scaled by the number of degrees of freedom, is 9.2. At the zeroth

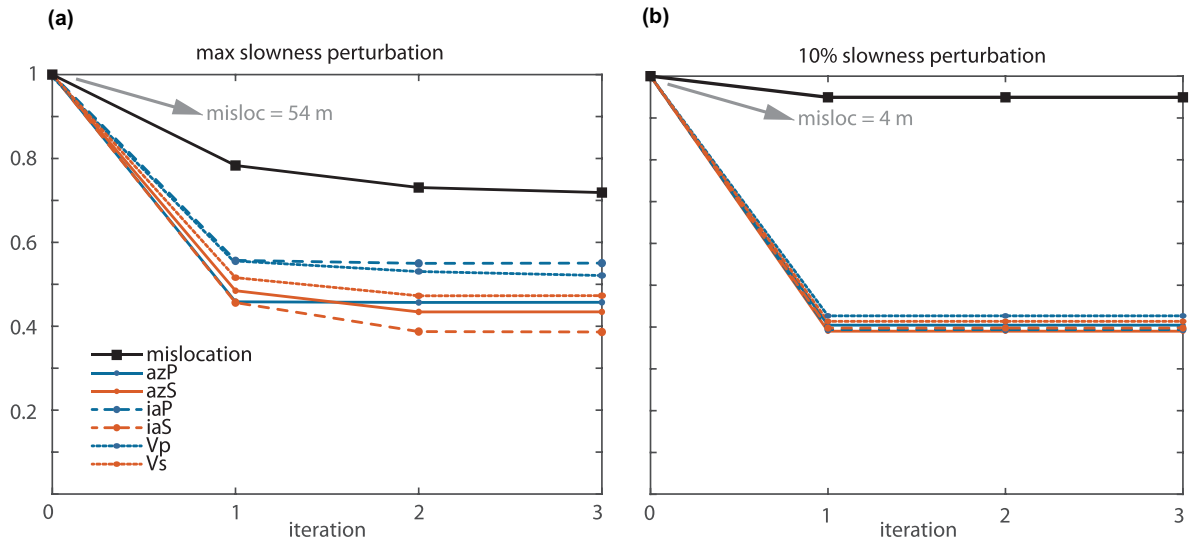

Figure 5. Results of synthetic tests with maximum allowed perturbation of the slowness vector (a) and 10 per cent perturbation of that (b). All curves represent average result over 100 realizations with different random perturbations. The black line is the spatial mislocation in terms of average distance between true and predicted locations. Blue and orange lines are the std (with respect to the true slowness) of the different slowness components, iteration by iteration. The arrows point to the absolute mislocations after the initial iteration.

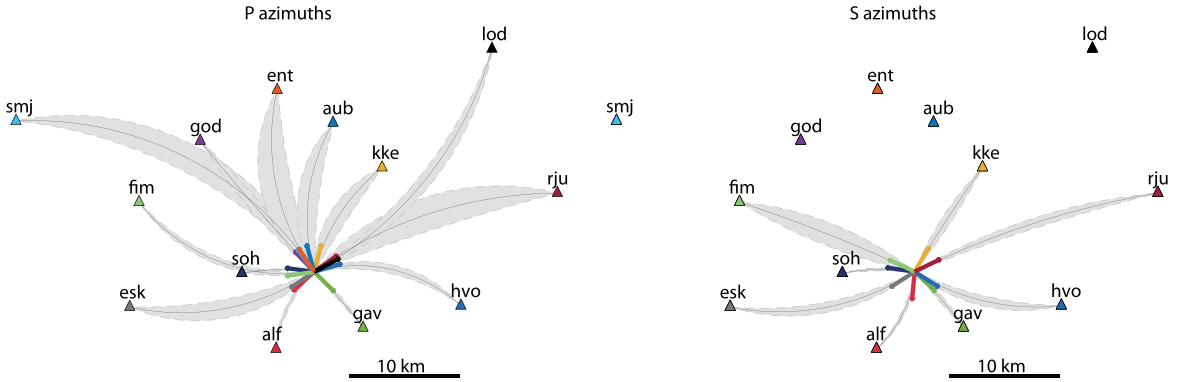

Figure 6. Average azimuth vectors and their std for all eight inversions performed, with different starting slowness vectors. *P* and *S* azimuths are drawn separately, as the inversion is performed separately.

iteration, it ranges for the eight inversions between 4.9 and 5.5, with larger values for larger slowness perturbations. After seven iterations, the misfit is reduced to values between 2.8 and 3.1.

All inversions converge to a similar size and shape of the cloud of hypocentres and the slowness vector components move in the same direction. However, they do not converge to the same values, as observed in Fig. 6 where the resulting azimuth angles are reported as average over the eight inversions and corresponding std. The results indicate that the variation increases with distance between station and seismic cluster. This is expected, as scattering effects are likely to increase for longer travel-distance, together with the width of the Fresnel zone. In some cases, the *P* and *S* azimuth angles move to opposite directions compared to the initial value. Also, for *P* waves the azimuths deviate more from straight paths, compared to *S* waves. The fact that the *P* and *S* waves appear to refract significantly differently to some of the stations in the network is surprising at first thought. However, neither our primary nor our secondary wave packets are pure body waves, as is clear from their non-linear particle motions.

The variation in spatial location between the initial (resulting from inversion for location parameters only, with fixed slowness) and final iteration (resulting from inversion for both location and slowness) is shown in Fig. 7. This comparison can be used to examine the difference between our method and common relative location methods that are based on 1-D velocity model, for example, HypoDD (Waldhauser & Ellsworth 2000). At the initial iteration all methods are the same in principle (in the case of a very small cluster where the slowness can be considered constant for all events) and results, therefore, have to be very similar, except for different inversion strategies (e.g. solving the inversion with an approximate solver or explicitly). In the following iterations, results become different between our method and the others because of the added flexibility about slowness. While in a 1-D velocity model hypocentres will not change significantly (because the cluster is small and there is no significant change in partial derivatives), with our method they do because we attempt to model refraction effects of 3-D velocity variations. Although these changes are small, they are significant and allow us to significantly reduce misfit and relative uncertainty. We estimated the significance of location movements by summing the squared lengths of the displacements normalized by their uncertainty over all events. If the displacements are random according to a Normal distribution and within the uncertainty, this quantity is χ^2 distributed for the appropriate number of degrees of freedom (NDF). Its expectation would be the NDF. Therefore, we normalize

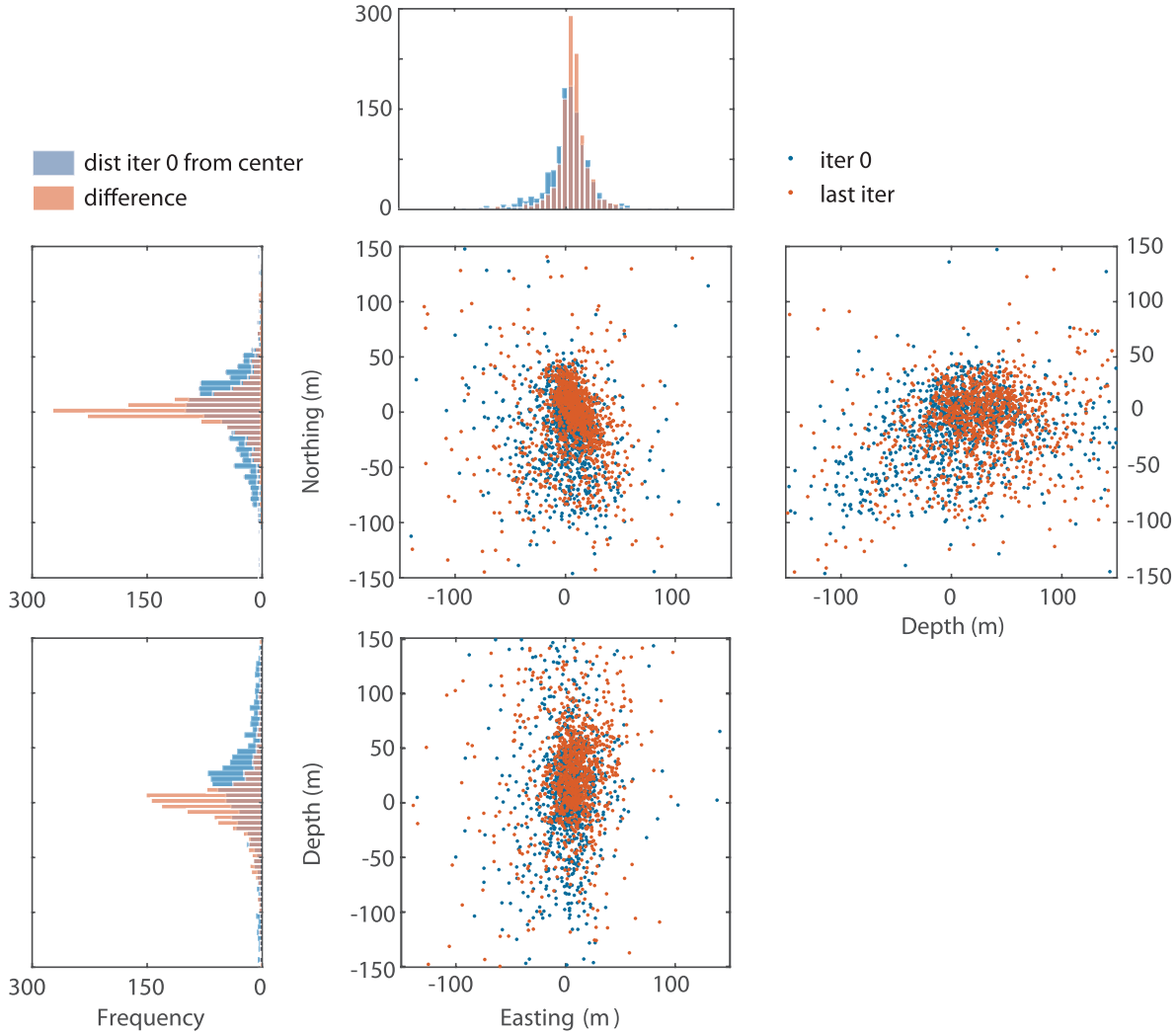

Figure 7. Comparison of locations after the initial (0th) and final iterations. The scatter plots to the right show cross sections as indicated through the cluster of events. Locations after the 0th iteration in orange and after the final iteration in blue. The histograms show the distributions of distance from the common centre of mass after the initial iteration in blue and the distribution of distances of event movements between the initial and final iteration in orange.

this quantity with the NDF and call it Q. The result for the initial iteration is $Q_{\text{initial}} = 7.1$. The result for the total movements in the remaining iterations is $Q_{\text{further}} = 1.8$. This shows that most of the movement occurs in the initial iteration and those movements are quite significant. The further movements are also clearly significant.

Final location results are shown in Figs 8 and 9. Fig. 8 shows a comparison of the absolute IMO catalogue locations, absolute non-linear locations obtained by Sgattoni *et al.* (2016) and the relative locations obtained in this study. The spatial distribution of 870 catalogue locations spans an area several km wide, with a formal uncertainty on the order of 1 km. The non-linear locations of 32 events, obtained with the addition of two temporary stations within 2 km from the cluster, are concentrated in a smaller area, less than 1 km wide, with uncertainty estimates around 400 m. Our relative locations of 1140 events cover an even smaller area, few hundred meters wide, with horizontal relative uncertainty on the order of 15–40 m (Figs 8 and 9).

The std estimates for the three spatial components (Fig. 10) indicate that the uncertainty in depth is about twice that in the horizontal directions. There are also changes with time: starting from January 2012 the std increases sharply in all directions and its variability increases. This correlates with changes in correlation coefficient and related data uncertainty estimates and the decrease in the number of observations per event (Fig. 4). Changes in network configuration, instead, do not appear to be correlated. In Fig. 9, we report the locations and error bars for all events (950) with a smaller std than 60 m on all three directions. The average std on the horizontal components corresponds to 14 m before January 2012 and 33 m after that. The average std in depth increases from 32 m to 45 m. In order to estimate the size of the cluster, we derive the combined probability density distribution of the whole cluster by summing the distribution of all individual events (based on their location uncertainties). Although visually the size of the cluster appears to increase in the second time period (after January 2012; Fig. 9), there is in fact no significant change, since the uncertainty increases as well. The resolved size of the cluster is estimated to be on the order of $25 \times 50 \times 100$ m^3 (easting, northing, depth). There is indication of a shift in location between the two time periods on the order of 30 m towards south, but this is not resolved as it is below the level of uncertainty.

The temporal evolution of depth shows interesting features (Fig. 11): a systematic, gradual upward migration of hypocentres

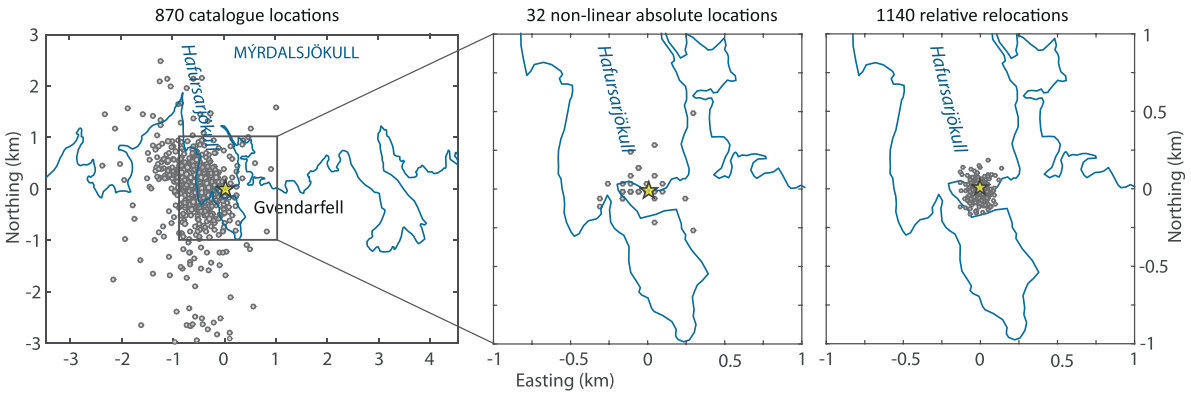

Figure 8. Map view of 870 events from the IMO catalogue, 32 nonlinear absolute locations (Sgattoni *et al.* 2016) and 1140 relative locations. The yellow star is the master event location, corresponding to the centre of the nonlinear absolute locations (at N63°32.772′, W19°05.988′ and depth corresponding to the local surface elevation) and is the origin of the axes scale. The blue line is the glacier outline derived from LiDAR DEM obtained in 2010 (Jóhannesson *et al.* 2013). The spatial distribution of the hypocentres is reduced with the relative location from several km to tens of m.

appears to be resolved, for a total of around 80 m, occurring between July and mid November 2011. Also, a period of unusually large variation is seen during the summer of 2012. Other smaller-scale, up and down shifts are also observed throughout the entire period. These, however, are not resolvable above the level of uncertainty.

7 DISCUSSION AND CONCLUSIONS

We have located with a relative location strategy around 1100 shallow, repeating LP seismic events located on Katla volcano's south flank, at Gvendarfell. This seismicity started in 2011, in coincidence with an unrest episode that culminated in a glacial flood and is characterized by a strikingly regular temporal pattern, with regular intervals between repeating seismic events, modulated by a seasonal variation. Sgattoni *et al.* (2016) suggested that this seismic activity may be related to hydrothermal processes, although no evidence for hydrothermal activity was found in the area. As they occur at the rim of the glacier, both volcanic and glacial processes must be taken into account as possible sources. Information on the size and shape of the seismic cluster may help constraining the source process. This motivated our detailed study in order to extract information on the hypocentre distribution.

The extreme similarity of all waveforms indicates a very small spatial distribution of hypocentres. In order to extract meaningful information about size and shape of the cluster, we have optimized the cross-correlation measurements and relative-location process in order to minimize uncertainty. With a synthetic test we have determined the best parameters for differential-time measurements and estimated their uncertainties, specifically for each waveform. This allowed avoiding further generalized statistical assumptions about errors.

We have then relocated the events with a master-event approach, which is justified by the small size of the problem: the waveforms are so similar that the master event is well correlated with all others. The 1-D velocity model assumption that is usually made in most location strategies is not likely to describe reality in volcanic areas where strong heterogeneities are expected. Therefore, we have designed the location strategy to work without a predefined velocity model, by formulating and inverting the problem to seek changes in both location and slowness. This strategy accounts for azimuth, take-off angles and velocity deviations from a 1-D model and allowed us to considerably improve the data fit. When allowing the slowness vectors to be changed during the inversion, the misfit is reduced by almost 50 per cent and approaches its expected value. In order to propagate data errors through the calculation, we have solved the inversion explicitly and estimated a location covariance matrix.

Our method is designed for a specific application, our data set at Katla and others similar. It exploits a specific feature of our data set, namely that the source region can be assumed to be so small that the sensitivity of travel time to changes in source location stay the same for all events. This specific geometrical circumstance allows us to include the simplest effects of 3-D heterogeneity, that is, those described by ray theory as refraction. This is significant in our case because the level of heterogeneity is expected to be high and this allows us to explain our data significantly better than when we do not allow for this flexibility. Similar circumstance is likely to arise in other volcanic regions where the level of heterogeneity is also high and microearthquakes are often densely clustered.

We have tested the program synthetically and observed a trade-off between locations and slowness that lies in the nature of the problem, which is non-linear and in which the model parameters are coupled as factors in the same term (eq. 4). For this reason, we have performed the inversion with several initial slowness vectors. All inversions resulted in similar hypocentre distributions and slowness values and angles.

The Gvendarfell seismic cluster appears to be distributed over a volume with depth distribution on the order of 100 m and horizontal distribution on the order of 25 × 50 m^2. This allows some considerations about the interpretation of the source:

(1) there is no suggestion that the shape of the cluster has a single plane-like geometry. Therefore, there is no evidence that the seismic events are generated by fault movement, despite the fact that a recent fault was identified in the area (Sgattoni *et al.* 2014). However, a planar shape cannot be excluded as the estimated uncertainty is significant and may prevent us from seeing an existing shape. Although it is more common for volcano-tectonic events to originate along faults, LP events may originate on rupture planes too (e.g. slow rupture failure in unconsolidated volcanic materials; Bean *et al.* 2014) and we cannot exclude that the low-frequency content is at least partly due to path effects. Also, if these events are generated by hydrothermal processes (Sgattoni *et al.* 2016), then they would be associated with permeability. Permeability in geothermal areas in Iceland is strongly connected with fracture zones;

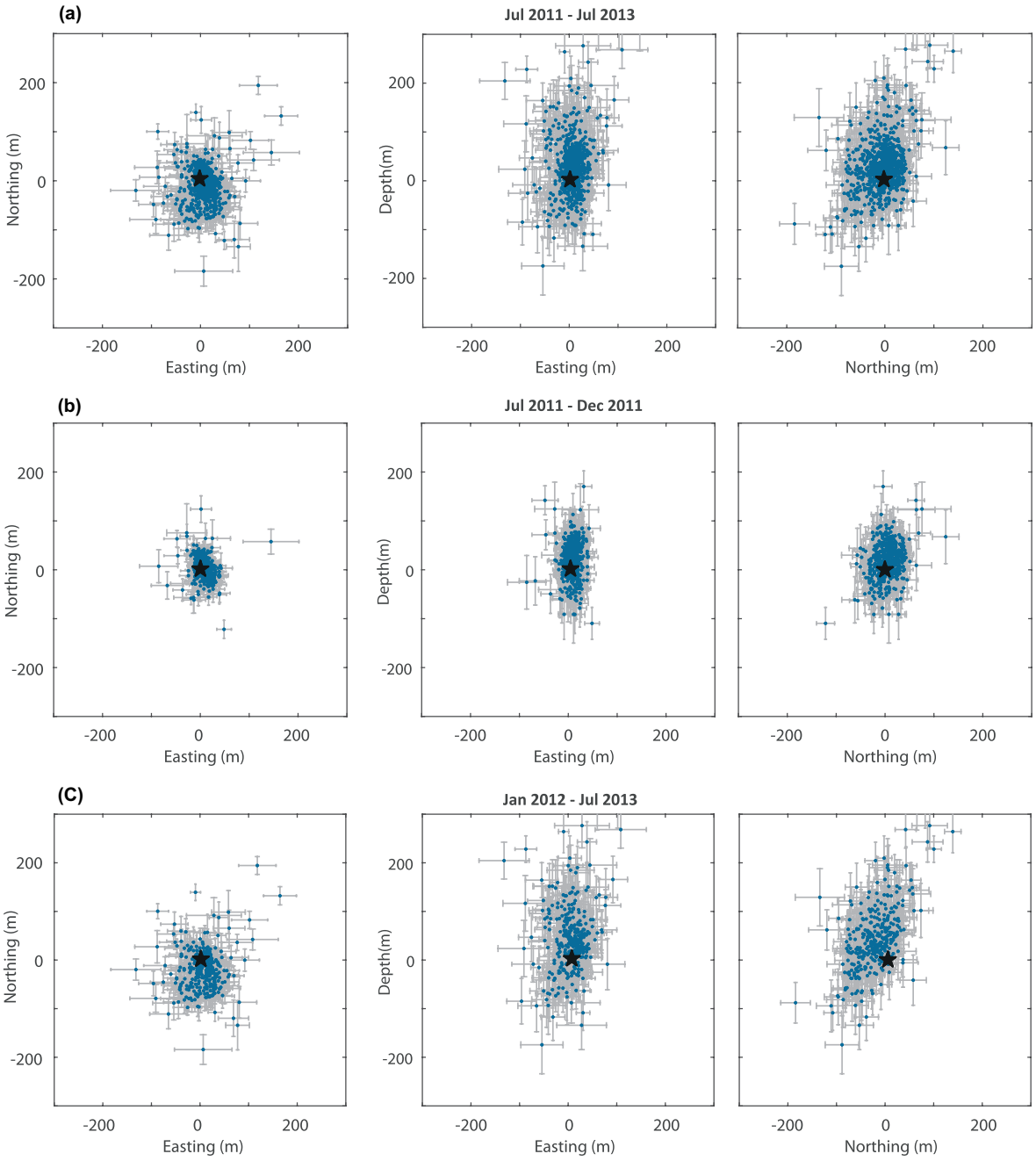

Figure 9. Relative location results for all events with a smaller std than 60 m in all directions. Blue points are the locations and grey lines represent uncertainty (± std). The star is the master event location, corresponding to the origin point of the axes. (a) 950 events for the entire time period (July 2011 and July 2013). (b) 550 events, until December 2011. (c) 400 events, from January 2012.

(2) the depth distribution of the hypocentres suggests that these events are unlikely to be generated by glacial processes, as the ice thickness is not expected to exceed few tens of meters in the area where the cluster is located. Therefore, volcano-related processes, magmatic or hydrothermal, are more likely, as suggested also by Sgattoni *et al.* (2016);

(3) the size and shape of the cluster do not exclude or point to a specific volcano-related source. In the case of a hydrothermal source, the size may be consistent with e.g. a crack or a crack volume filled with hydrothermal fluid. Alternatively, a small batch of magma rising at shallow depth may act as a source. The size of the cluster is consistent with the size of silicic magma bodies identified in the Gvendarfell area (Sgattoni *et al.* 2014).

Some indications of minor temporal changes are suggested by decreased cross-correlation coefficient and increased location uncertainty after January 2012. While the location uncertainty may be influenced by e.g. network configuration changes, a systematic decrease in correlation coefficient may be associated with a decrease in the size of the events or with changes in either source process or hypocentre locations. There is no clear correlation between magnitude and correlation coefficient variations or between

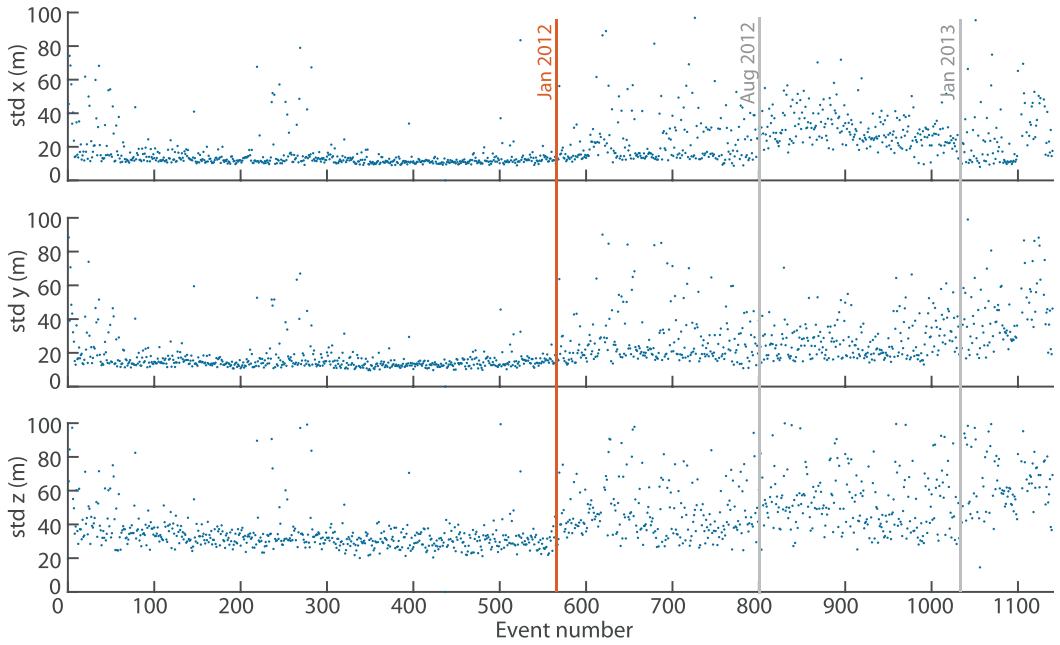

Figure 10. Time history of estimated uncertainty (std) of relative locations with changes highlighted with time-labelled vertical bars. Estimated std of the spatial coordinates of the relative location: x (easting), y (northing), z (depth). A clear increase occurs in January 2012 and peaks in August 2012. The orange bar to the left indicates the time separation used in Fig. 9.

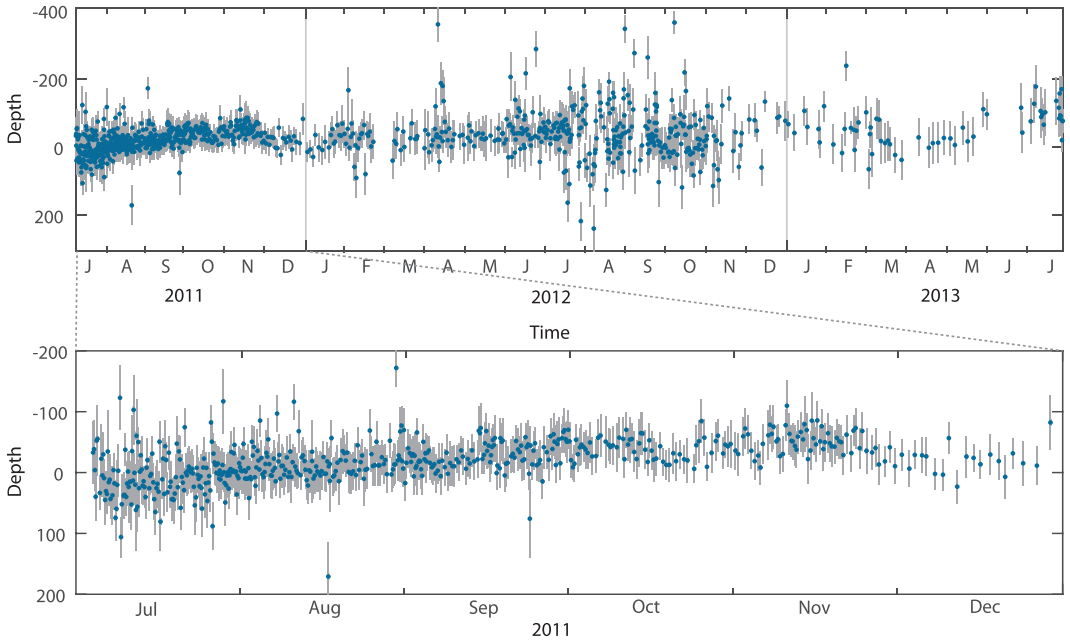

Figure 11. Time history of depth for the entire time period (top) and for the July–December 2011 time interval (bottom). Blue dots are depth as a function of time and grey bars are the corresponding standard deviations.

the systematic increase in location uncertainty and the changes in the network configuration. We suggest, therefore, that time changes in either the source process or hypocentre location may have occurred starting from January 2012. There is an indication of a shift of the hypocentres towards south, but this is below the uncertainty level. Greater and more systematic location changes are observed in depth, in particular in the first 5 months, when a gradual upward migration of hypocentres occurs, reaching a maximum of 80 m. It is not straightforward to infer what this time changes would imply for the source interpretation. A source involving movements of a fluid phase like that suggested by Sgattoni *et al.* (2016) may be consistent with such location shifts.

ACKNOWLEDGEMENTS

The authors would like to thank the Icelandic Meteorological Office for access to waveform data. The temporary deployments producing data for this study were supported by CNDS (Centre for Natural Disaster Science, http://www.cnds.se) at Uppsala University and

the Volcano Anatomy project, financed by the Icelandic Science Foundation. This work was funded by the University of Bologna, University of Iceland and Uppsala University, as a part of a joint PhD project. We thank Joachim Wassermann, Ragnar Slunga and an anonymous reviewer for the valuable comments that helped to improve this paper.

REFERENCES

Aki, K. & Richards, P., 1980. *Quantitative Seismology: Theory and Methods,* W. H. Freeman.

Bean, C.J., De Barros, L., Lokmer, I., Métaxian, J.-P., O'Brien, G. & Murphy, S., 2014. Long-period seismicity in the shallow volcanic edifice formed from slow-rupture earthquakes, *Nat. Geosci.,* **7,** 71–75.

Chouet, B., 2003. Volcano seismology, *Pure appl. Geophys.,* **160**(3), 739–788.

Deichmann, N. & Garcia-Fernandez, M., 1992. Rupture geometry from high-precision relative hypocentre locations of microearthquake clusters, *Geophys. J. Int.,* **110**(3), 501–517.

Fréchet, J., 1985. ogenése et doublets sismiques, *Master's thesis,* Université Scientifique et Médicale de Grenoble, Grenoble, France.

Frémont, M.-J. & Malone, S.D., 1987. High precision relative locations of earthquakes at Mount St. Helens, Washington, *J. geophys. Res.,* **92**(B10), 10 223–10 236.

Geller, R.J. & Mueller, C.S., 1980. Four similar earthquakes in central California, *Geophys. Res. Lett.,* **7**(10), 821–824.

Got, J.-L., Fréchet, J. & Klein, F.W., 1994. Deep fault plane geometry inferred from multiplet relative relocation beneath the south flank of Kilauea, *J. geophys. Res.,* **99**(B8), 15 375–15 386.

ITO, A., 1985. High resolution relative hypocenters of similar earthquakes by cross-spectral analysis method, *J. Phys. Earth,* **33**(4), 279–294.

Jeddi, Z., Tryggvason, A. & Gudmundsson, O., 2016. The Katla volcanic system imaged using local earthquakes recorded with a temporary seismic network, *J. geophys. Res.,* in press, doi:10.1002/2016JB013044.

Jóhannesson, T., Björnsson, H., Magnússon, E., Guðmundsson, S., Pálsson, F., Sigurðsson, O., Thorsteinsson, T. & Berthier, E., 2013. Ice-volume changes, bias estimation of mass-balance measurements and changes in subglacial lakes derived by lidar mapping of the surface of icelandic glaciers, *Ann. Glaciol.,* **54**(63), 63–74.

Lees, J.M., 1998. Multiplet analysis at coso geothermal, *Bull. seism. Soc. Am.,* **88**(5), 1127–1143.

Michelini, A. & Lomax, A., 2004. The effect of velocity structure errors on double-difference earthquake location, *Geophys. Res. Lett.,* **31**(9), L09602, doi:10.1029/2004GL019682.

Poupinet, G., Ellsworth, W.L. & Frechet, J., 1984. Monitoring velocity variations in the crust using earthquake doublets: an application to the Calaveras fault, California, *J. geophys. Res.,* **89**(B7), 5719–5731.

Rowe, C., Thurber, C. & White, R., 2004. Dome growth behavior at Soufriere hills volcano, Montserrat, revealed by relocation of volcanic event swarms, 1995–1996, *J. Volcanol. Geotherm. Res.,* **134**(3), 199–221.

Scherbaum, F. & Wendler, J., 1986. Cross spectral-analysis of Swabian Jura (SW Germany) 3-component microearthquake recordings, *J. Geophys.,* **60**(3), 157–166.

Sgattoni, G., Einarsson, P., Lucchi, F., Gudmundsson, O., De Astis, G. & Tranne, C.A., 2014. A new source of seismic events on Katla volcano's south flank, *Geophysical Research Abstract,* **16,** EGU2014–543.

Sgattoni, G., Jeddi, Z., Gudmundsson, O., Einarsson, P., Tryggvason, A., Lund, B. & Lucchi, F., 2016. Long-period seismic events with strikingly regular temporal patterns on Katla volcano's south flank (Iceland), *J. Volcanol. Geotherm. Res.,* **324,** 28–40.

Slunga, R., Rognvaldsson, S.T. & Bodvarsson, R., 1995. Absolute and relative locations of similar events with application to microearthquakes in southern iceland, *Geophys. J. Int.,* **123**(2), 409–419.

Thelen, W., Crosson, R. & Creager, K., 2008. Absolute and relative locations of earthquakes at Mount St. Helens, Washington, using continuous data: implications for magmatic processes, in *A Volcano Rekindled: the Renewed Eruption of Mount St. Helens, 2004–2006,* pp. 71–89, eds Sherrod, D.R., Scott, W.E. & Stauffer, P.H., U.S. Geological Survey Professional Paper.

VanDecar, J.C. & Crosson, R.S., 1990. Determination of teleseismic relative phase arrival times using multi-channel cross-correlation and least squares, *Bull. seism. Soc. Am.,* **80**(1), 150–169.

Waldhauser, F. & Ellsworth, W.L., 2000. A double-difference earthquake location algorithm: method and application to the northern hayward fault, california, *Bull. seism. Soc. Am.,* **90**(6), 1353–1368.

Wolfe, C.J., 2002. On the mathematics of using difference operators to relocate earthquakes, *Bull. seism. Soc. Am.,* **92**(8), 2879–2892.